Author Manuscript

Author Manuscript

Author Manuscript

Author Manuscript

HHS Public Access

Author manuscript

Magn Reson Med. Author manuscript; available in PMC 2017 March 01.

Published in final edited form as:

Magn Reson Med. 2017 March ; 77(3): 1193–1200. doi:10.1002/mrm.26177.

Dual-pathway sequences for MR thermometry: When and where to use them

Pelin Aksit Ciris[1,2], **Cheng-Chieh Cheng**[2], **Chang-Sheng Mei**[3], **Lawrence P. Panych**[2], and **Bruno Madore**[2]

[1] Department of Biomedical Engineering, Akdeniz University, Antalya Turkey

[2] Department of Radiology, Brigham and Women's Hospital, Harvard Medical School, Boston, MA, USA

[3] Department of Physics, Soochow University, Taipei, Taiwan

Abstract

Purpose—Dual-pathway sequences have been proposed to help improve the temperature-to-noise-ratio (TNR) in MR thermometry. The present work establishes how much of an improvement these so-called 'PSIF-FISP' sequences may bring in various organs and tissues.

Methods—Simulations and TNR calculations were validated against analytical equations, phantom, abdomen and brain scans. Relative TNRs for PSIF-FISP, as compared to a dual-FISP reference standard, were calculated for flip angle (FA) = 1 to 85° and TR = 6 to 60ms, for gray matter, white matter, cervix, endometrium, myometrium, prostate, kidney medulla and cortex, bone marrow, pancreas, spleen, muscle, and liver tissues.

Results—PSIF-FISP was TNR superior in the kidney, pelvis, spleen or gray matter at most tested TR and FA settings, and benefits increased at shorter TRs. PSIF-FISP was TNR superior in other tissues, e.g. liver, muscle, pancreas, for only short TR settings (20ms or less). The TNR benefits of PSIF-FISP increased slightly with FA, and strongly with decreasing TR. Up to 2-3 fold reductions in TR with 20% TNR gains were achievable. In any given tissue, TNR performance is expected to further improve with heating, due to changes in relaxation rates.

Conclusion—Dual-pathway PSIF-FISP can improve TNR and acquisition speed over standard GRE sequences, but optimal acquisition parameters are tissue dependent.

Keywords

MR thermometry; Multi-pathway sequences; temperature-to-noise-ratio; PSIF; DESS; proton resonance frequency shift

Corresponding Author: Dr. Chang-Sheng Mei, Soochow University, Department of Physics, 70 Linhsi Road, Taipei, TW (R.O.C.).

Author Manuscript Author Manuscript Author Manuscript Author Manuscript

Introduction

MR thermometry is valuable for monitoring and guiding thermal therapies, as it can detect temperature changes in a noninvasive manner (1,2). The most common MR thermometry approach is based on the proton-resonant-frequency (PRF) shift of water signals (3-7).

Safety and efficacy of thermal therapies require accurate temperature measurements with high temperature-to-noise-ratio (TNR), as well as high spatial and temporal resolution (8). PRF temperature maps are typically constructed by measuring phase changes using gradient-recalled echo (GRE) sequences (4,6).

There exist many different types of GRE sequences, most of which are sensitive to the PRF effect. GRE sequences can be spoiled (e.g., FLASH, SPGR), unbalanced steady-state (e.g., FISP, GRASS) or balanced steady-state (e.g., True-FISP, balanced-SSFP, balanced-FFE, FIESTA), and their readout can be of an EPI, single-line, spiral, radial or just about any other type. Spoiled sequences represent a common and reasonable choice for PRF thermometry; however, their signal becomes vanishingly small as TR approaches zero, and short TR settings can prove useful in some situations, for example when faster scanning and/or improved motion robustness might be required. In contrast, unbalanced steady-state sequences can effectively capture the PRF effect while maintaining high signal levels even at very short TR settings.

A particular type of unbalanced steady-state sequence, a dual-pathway sequence, was proposed to improve TNR over standard GRE sequences (9,10) . It is based on the fact that the two typically-strongest signal pathways in steady-state sequences, the ‘fast imaging with steady-state free precession’ (FISP) and the inverted-FISP (PSIF) pathways, have maximum temperature sensitivity at different moments in the TR period: The PSIF is maximally sensitive early in TR, and the FISP late in TR. The purpose of the present study was to quantify how much of a TNR improvement can be expected from such dual-pathway sequence in various imaging conditions and tissue types. Recommendations were developed as to where and when to use dual-pathway sequences for MR thermometry, as validated in phantom and *in vivo* experiments.

Methods

The dual-pathway sequence considered here samples a so-called PSIF signal early in the TR period and a FISP signal late in TR (9). This sequence is similar to ‘dual-echo steady state’ (DESS) (11) except for the order of the PSIF and FISP echoes which is inverted here, to sample each signal when it is maximally sensitive to temperature (9). Experimentally testing the sequence in a wide range of imaging conditions and tissue types would not be practical, and for this reason our final results and recommendations are based on simulations. As described below, experiments were designed to validate the simulation in a number of different contexts, to build confidence in the final (simulated) results.

Author Manuscript Author Manuscript Author Manuscript Author Manuscript

A. Simulations – Overall description

With any unbalanced steady-state sequence, all magnetization pathways are present at all times, but most are displaced to far-away regions of k-space where they may be ignored. In numerical simulations, arbitrary spatial resolution can be achieved, meaning that an arbitrarily-large k-space extent including many different signal pathways can readily be captured. A homogeneous 1D object with no k-space feature of its own (beyond a delta function) was simulated with great resolution, so that a Fourier transform could reveal several distinct pathway signals. Each simulated voxel contained many isochromats, with Lorentzian frequency distribution. At the onset all isochromats pointed along the *z* direction; the simulation program then applied rotation matrices to simulate RF pulses, imaging gradients and offset-frequency effects, T_1 recovery was applied along *z*, and $T_2 = 1/R_2$ decay was applied along *x* and *y*. This T_2 decay, combined with a loss of coherence among isochromats, led to a $T_2^*=1/\left(R_2+R_2^{'}\right)$ decay for positive-pathway signals (e.g., FISP). In contrast, negative pathway signals (e.g., PSIF) behaved according to $1/\left(R_2-R_2^{'}\right)$ as expected (12). At every sampling window the object's signal was Fourier transformed and the appropriate pathway signals captured. The RF phase alternated by 180° every TR, and a half-flip angle excitation in the first TR was used to accelerate the approach to steady-state. The first 500 excitations were discarded to ensure steady-state was reached even for the shortest TR and/or longest T_1 settings. All calculations were performed in Matlab (Mathworks, Natick, MA).

B. Validation against analytical solutions $\left(R_2^{'}=0\right)$

With no reversible decay component, i.e., $R_2^{'}=0$ and $T_2^*=T_2$, PSIF and FISP signal is given analytically by (13-15):

$$S_{FISP}\left(TE\right)=M_0\,tan\left(\frac{\theta}{2}\right)\left(1-\left(E_1-cos\left(\theta\right)\right)\times R\right)\times e^{-TE/T_2}, \quad [1]$$

$$S_{PSIF}\left(TE\right)=M_0\,tan\left(\frac{\theta}{2}\right)\left(\frac{1-\left(1-E_1\,cos\left(\theta\right)\right)\times R}{E_2}\right)\times e^{-TE/T_2} \quad [2]$$

, where θ and M_0 are the flip angle (FA) and equilibrium magnetization, respectively, and:

$$E_1=e^{-TR/T_1} \quad [3]$$

,

$$E_2=e^{-TR/T_2} \quad [4]$$

Author Manuscript Author Manuscript Author Manuscript Author Manuscript

,

$$R = \sqrt{\left(1 - E_2^2\right) / \left(\left(1 - E_1 \cos\left(\theta\right)\right)^2 - \left(E_2 \times \left(E_1 - \cos\left(\theta\right)\right)\right)^2\right)} \quad [5]$$

. Simulations and calculations used $TE_{PSIF} = TR/4$, $TE_{FISP} = 3\ TR/4$ and the parameter ranges: T_1 = 350 to 1850ms, T_2 = 12 to 140ms, θ = 5 to 85°, TR = 6 to 60ms, with 15 evenly-spaced values in each range. Each parameter was simulated in turn, over its whole range, while other parameters were kept constant in the middle of their own range.

C. Validation against phantom data $\left(R_2' \neq 0\right)$

Tubes of agar gel were doped with manganese sulfate (MnSO4): 1000, 670, 500, 330, or 170ppm, and had T_1, T_2 and T_2^* values as listed in Table 1. This five-tube phantom was imaged with our PSIF-FISP sequence and a dual-FISP sequence. Sixteen combinations of imaging parameters were employed: four different FA settings for each one of four different combinations of TR and TE, as listed in Table 2. Other imaging parameters included: EPI readout with echo-train-length (ETL)=24, FOV=18×13.5cm^2, in-plane resolution=1.4×1.4mm^2, slice thickness=5mm, 8-channel head coil. For each magnitude image i, a noise ROI was placed in the background, $R_{N,i}$. Similarly, signal ROIs were placed on each tube j, $R_{S,i,j}$. To reduce bias in estimating magnitude signal and noise levels the following correction scheme was applied (16):

$$M_{N,i} = std\left(R_{N,i}\right) / \sqrt{2 - \pi/2} \quad [6]$$

,

$$M_{S,i,j} = \sqrt{abs\left(\text{mean}\left(R_{S,i,j}\right)^2 - {M_{N,i}}^2\right)} \quad [7]$$

, where $M_{N,i}$ and $M_{S,i,j}$ represent corrected noise and signal levels for image i and tube j, respectively, with $1 \leq i \leq 16$ for all sixteen imaging schemes and $1 \leq j \leq 5$ for all five phantom tubes described above. A matching set of 160 (i.e., 5 tubes × 16 scans × 2 sequences) simulations were performed, for comparison purposes, using the known pulse sequence parameters and relaxation rates of each tube. To simulate the slice profile, FAs from θ = 0° up to the prescribed value were simulated in steps of 0.1°, and results were combined with Gaussian weighting.

Three separate scaling factors were needed when comparing the 160 measured $M_{S,i,j}$ values to their simulated counterparts. A fit parameter scaled M_0, which is bound to have a different numerical value in simulations vs. experiments. A second fit parameter accounted for the receive coil having different B_1 sensitivity for different tubes, as they were at different locations within the coil. A third one scaled the nominal FA, to account for variations in

Author Manuscript Author Manuscript Author Manuscript Author Manuscript

transmit B_1^+ values. Unconstrained non-linear least-square fits were performed with the Matlab 'lsqnonlin' function. Bland-Altman plots were generated to compare experimental and simulation results.

D. Validation against *in vivo* abdomen results $\left(R_2' \neq 0\right)$

Abdominal imaging was performed on three healthy subjects at 3T (Signa HDxt Twin Speed, GE Healthcare), following informed consent using an IRB-approved protocol. Four scans were performed on each subject with varying ETL, TR and TE settings (Table 2). Other parameters included: θ=30°, FOV=24×18cm^2, in-plane resolution=1.88×1.88mm^2, slice thickness=5mm, 8-channel coil.

Three ROIs were drawn for each scan from each subject: one including all visible kidney tissue, another including all visible liver tissue (excluding blood vessels), and a third in the noise background. Corrected signal and noise levels were obtained as described in Eq. 6 and 7. Simulations for all 24 cases (3 subjects × 4 scans × 2 organs) were performed using the known imaging parameters and literature values for relaxation times ((17,18), Table 1). Equal contributions from kidney cortex and medulla tissues were assumed, i.e., cortex and medulla results were averaged to generate simulated kidney results. As before, FAs ranging from θ=0° to the nominal FA setting of 30° were simulated and combined with Gaussian weighting. Two fit parameters were employed, for M_0 and receive-B_1 scaling.

E. Validation against *in vivo* brain results $\left(R_2' \neq 0\right)$

Brain imaging was performed on four healthy subjects at 3T (Siemens Skyra), following informed consent using an IRB-approved protocol (30.4 ± 2.1 yo). A single axial whole-brain 3D scan was performed on each subject, but each scan sampled several PSIF and several FISP echoes during each TR period. These scans were performed in the context of our prior work (12,19) where we showed that T_2 and T_2^* maps can be calculated from such data. The number of slices, FA, TR and TE settings varied slightly across subjects (Table 2). Other parameters included: FOV=19.2×19.2cm^2, in-plane resolution=1×1×2mm^3, 32-channel head coil.

ROIs were drawn within white matter, caudate nucleus, putamen, globus pallidus, red nucleus, and substantia nigra tissues, for each subject. Signal levels in each ROI were simulated based on known imaging parameters, on calculated T_2 and T_2^* maps (12,19), and on literature values for T_1 ((20-22), Table 1). As part of the fitting procedure involved in calculating T_2 and T_2^* maps, PSIF and FISP signal levels at TE=0 were also calculated (12, 19) from the *in vivo* data, and compared to simulation results. FA values were assumed uniform within each ROI in the 3D volume. As before, two fit parameters were employed, for M_0 and receive-B_1 scaling.

F. TNR equation

The main purpose of the experiments from Sections B-E above was to validate our simulation software for the task of accurately predicting PSIF and FISP signal levels, in a

Author Manuscript Author Manuscript Author Manuscript Author Manuscript

variety of imaging conditions. An equation is derived below to convert such PSIF and FISP signal levels into a measure of TNR, using the dual-FISP sequence as a reference standard.

The temperature sensitivity for FISP and PSIF signals, Λ_{FISP} and Λ_{PSIF}, is given by (9):

$$\Lambda_{FISP}=\alpha\times\gamma\times B_0\times TE_{FISP},\quad \Lambda_{PSIF}=\alpha\times\gamma\times B_0\times(TR-TE_{PSIF}) \quad [8]$$

, where $\gamma = 2\pi\times 42.58$ MHz/T is the gyromagnetic ratio for hydrogen and $\alpha=-0.01$ ppm/°C is the proton resonance frequency change coefficient. Phase shifts from either FISP or PSIF signals, $\Delta\phi_{FISP}$ or $\Delta\phi_{PSIF}$, can provide relative temperature measurements:

$$\Delta T_{FISP}=\Delta\phi_{FISP}/\Lambda_{FISP}, \Delta T_{PSIF}=\Delta\phi_{PSIF}/\Lambda_{PSIF} \quad [9]$$

. With multi-pathway sequences, such as the PSIF-FISP or the dual-FISP sequences considered here, measurements from the individual pathways are combined with proper weights, to obtain a TNR-optimum estimate (9):

$$\Delta T_{PSIF-FISP}=(\Delta T_{PSIF}\times W_{PSIF}+\Delta T_{FISP}\times W_{FISP})/(W_{PSIF}+W_{FISP}) \quad [10]$$

$$\Delta T_{dual-FISP}=(\Delta T_{FISP1}\times W_{FISP1}+\Delta T_{FISP2}\times W_{FISP2})/(W_{FISP1}+W_{FISP2}) \quad [11]$$

. Assuming all FISP and PSIF images have the same noise statistics (i.e., same imaging bandwidth, matrix size, acceleration, scaling) these weights are simply given by:

$$W_{PSIF}=(S_{PSIF}\times\Lambda_{PSIF})^2,\quad W_{FISP}=(S_{FISP}\times\Lambda_{FISP})^2 \quad [12]$$

. Weights for PSIF or FISP signals in a dual-pathway sequence, or for the first and second FISP in a dual FISP sequence, differ because both their signal intensity and temperature sensitivity may differ, as shown in Eqs. 8 and 12. Worth noting, because any estimate of S_{PSIF} and S_{FISP} will include noise, the weights from Eq. 12 may in practice only approach optimal ones.

The relative TNR, *E,* of our PSIF-FISP sequence, as compared to a dual-FISP sequence, depends only on the weights from Eq. 12:

$$E=\sqrt{\frac{W_{PSIF}+W_{FISP}}{W_{FISP1}+W_{FISP2}}} \quad [13]$$

, Note that no ΔT term appears in Eq. 13, i.e., E is independent of the actual temperature change being measured. A slightly different version of Eq. 13 is also of interest here:

Author Manuscript Author Manuscript Author Manuscript Author Manuscript

$$E_{global}=\frac{\sqrt{W_{PSIF}+W_{FISP}}}{max\left(\sqrt{W_{FISP1}+W_{FISP2}}\right)} \quad [14]$$

, where the max(·) function is applied over all simulated imaging parameters. While E in Eq. 13 compares a PSIF-FISP sequence to a dual-FISP sequence for a given set of imaging parameters, E_{global} in Eq. 14 compares it instead to the very best the dual-FISP sequence can offer, i.e., it compares PSIF-FISP results for given acquisition parameters to an optimized version of the dual-FISP sequence.

G. Validation against Monte Carlo simulations

Monte Carlo simulations were performed to validate Eq. 13. Varying amounts of noise were added to simulated data and relative TNRs were calculated to obtain a Monte Carlo equivalent of E, called E_{MC} below.

More specifically, noisy pre-heating signals were generated by adding normally distributed random noise to the real and imaginary signals from each pathway. Post-heating signals were generated by adding heat-induced phase shifts to the simulated pre-heating signals, and normally-distributed random noise was added to both pre- and post-heating signals, in both real and imaginary channels. Temperature estimates were obtained by dividing phase differences with the temperature sensitivities given in Eq. 8. Finally, for each tissue, the relative TNR was obtained by dividing the temperature noise for PSIF-FISP with that for dual-FISP:

$$E_{MC}=std\left(\Delta T_{dual-FISP}\right)/std\left(\Delta T_{PSIF-FISP}\right) \quad [15]$$

. E_{MC} vs. E comparisons were performed for all combinations of the acquisition parameters θ = 40°, 60°, 80° and TR = 10, 15, 20ms, for several tissue types. T_1 and T_2 values are provided in Table 1. For all cases, $TE_1=TR/4, \quad TE_2=3 \quad TR/4, \quad T_2^*=T_2/2$ and 2D acquisitions were simulated using Gaussian slice profiles, as previously described.

H. TNR-based recommendations for various tissue types

The relative TNR, E, from Eq. 13, was calculated for a wide array of imaging parameters and tissue types based on simulated PSIF and FISP signals. All combinations of θ=1 to 85°, in steps of 1° and TR=6 to 60ms, in steps of 1ms, were simulated for a variety of acquisition parameters and tissue types. Color coding helped visualize cases where the PSIF-FISP sequence offers a boost in TNR (E>1, green) vs. TNR penalties (E<1, red). Black represented cases with E≈1, where PSIF-FISP and dual-FISP sequences were essentially equivalent TNR-wise.

A contour plot for E_{global}, from Eq. 14, was overlaid onto the color-coded rendering. The result was a compact display that thoroughly compared the TNR performance of PSIF-FISP and dual-FISP sequences: The PSIF-FISP sequence performed ‘better’ wherever the display

Author Manuscript Author Manuscript Author Manuscript Author Manuscript

is green, and contour plots helped determine how good, in global terms, the performance turned out to be.

Results

The dual-pathway simulations with $R_2'=0$ showed close agreement with the analytical solutions from Eq. 1-5 (Fig. 1a-d). Signal levels for a spoiled GRE sequence were also plotted; they typically proved weaker than those of the steady-state sequences considered here. At short TR settings, the signal levels from spoiled sequences can be order of magnitudes weaker than that of a steady-state sequence (as shown in Fig. 1d). Close agreement was also observed between E (Eq. 13) and its Monte Carlo counterpart E_{MC} (Eq. 15) for all simulated tissue types (Fig. 1e).

Simulations and experimental results, with $R_2' \neq 0$, also closely agreed in phantoms (Fig. 2a and Fig. 2d-g), in abdominal imaging (Fig. 2b), and in brain imaging (Fig. 2c). Scaling factors from the fits were as follows. Phantom: Transmit B_1^+ scaling 82% of nominal value and receive-B_1 scaling equal to 106%, 95%, 96%, 101%, and 116% for tubes A through E, respectively. Abdominal and neuro: Transmit B_1^+ scaling equal to nominal value, and receive-B_1 scaling equal to 95 ± 25% and 105 ± 8% over multiple subjects and scans for liver and kidney ROIs, respectively; and 106 ± 14%, 121 ± 18%, 119 ± 15%, 90 ± 12%, 109 ± 13% and 121 ± 14% over multiple subjects for white matter, caudate nucleus, putamen, globus pallidus, red nucleus, and substantia nigra ROIs, respectively. As could be expected, higher receive-B_1 scaling values corresponded to tubes and tissues located closer to the receive coil. Scaling factors for M_0 are not listed as they have no particular physical meaning.

Close agreement between analytical, simulated, Monte Carlo simulated and experimental data as shown in Figs 1 and 2 represented validation for the simulation software. In contrast, the simulated results in Fig. 3 intended to serve as recommendations for the choice of sequence and imaging parameters for PRF imaging. The PSIF-FISP strategy proved superior (green) compared to a more conventional FISP-FISP scheme for kidney, pelvis, spleen or gray matter imaging at most TR and FA settings, and benefits increased at shorter TRs. The PSIF-FISP strategy proved superior only for short TR settings in other tissues such as the liver, muscle or pancreas. In all cases, TNR benefits of the PSIF-FISP acquisition increased considerably as TR decreased, and slightly as FA increased. As can be seen from E_{global} contour lines in Fig. 3, for tissues that benefited most from PSIF-FISP (b-g), maximal dual-FISP TNR tended to occur at longer TR settings, e.g., >40ms. In such cases a 2-3 fold reduction in TR could be achieved with PSIF-FISP at minimal cost in TNR (Fig. 3b-g). In contrast, for tissues that benefited least from PSIF-FISP (Fig. 3h-n), maximal dual-FISP TNR occurred at shorter TR settings and PSIF-FISP had little more to offer.

Figure 3o shows the relative TNR of PSIF-FISP vs. dual-FISP as a function of T_1 and T_2 (TR=15ms, FA=60°). Again, tissues with longer T_1 and T_2 values tended to benefit most from PSIF-FISP (e.g., kidney, pelvis, spleen and gray matter), while advantages were more limited otherwise. It is worth noting that as tissues are heated causing T_1 and T_2 to increase,

Author Manuscript Author Manuscript Author Manuscript Author Manuscript

the relative TNR would also increase (Fig. 3o). T_1 increases by 1-2% per °C (23-25), and a nonlinear sigmoidal relationship between T_2 and temperature resulted in similar changes in T_2 per °C (26,27). For example, for a 20 °C increase in tissue temperature, from 37 °C to 57 °C, and a 1-2% change in T_1 and T_2 per °C, relative TNR for spleen and liver tissues would increase as shown in Fig. 3o: Using a low estimate of 1% for T_1 and T_2 per °C, relative TNR would increase by 2% with heating in spleen tissues (from 111 to 113%) and by 4% in liver tissues (from 101 to 105%), as indicated with yellow markings in Fig. 3o. Using a higher estimate of 2% per °C, relative TNR would increase by 4% in spleen (to 113%) and by 5% in liver (to 106%), as indicated with red markings in Fig. 3o.

Discussion

Excellent agreement was obtained between analytical, simulated and experimental results (Figs 1 and 2). Visual displays were presented to help guide the choice of pulse sequence and imaging parameters for PRF thermometry (Fig. 3). In general, dual-FISP sampling provided the highest TNRs at relatively long TR values, and may be a good choice if lower temporal/spatial resolution is acceptable. EPI readouts could help improve temporal resolution, at a cost in artifact content and geometrical fidelity. In contrast, a PSIF-FISP sampling strategy may be a fine option for faster scanning with shorter TR settings. The PSIF-FISP sampling strategy ensures that both PSIF and FISP components are acquired near their maximal temperature sensitivity, which leads to significant improvements in TNR, especially for tissues associated with longer relaxation times. Because both T_1 and T_2 are expected to increase with temperature (28-30), TNR advantages for the PSIF-FISP scheme are expected to increase in all tissue types as heating occurs (Fig. 3o).

The performance of the dual-pathway sequence was compared here to another steady-state acquisition, a dual-FISP sequence (e.g., Fig. 3). Both steady-state sequences would vastly outperform spoiled sequences such as FLASH or SPGR at short TR settings (as shown in Fig. 1d), but the TNR performance gap would vanish at long TR. As a consequence, the rationale for steady-state sequences in an MR thermometry application may be strongly linked to the desire, or lack thereof, for shorter TR settings and faster imaging.

T_2^* is not, strictly speaking, a property of tissues, as it depends to a large degree on geometry and shimming. A limitation of this study came from some of the T_2^* values not being precisely known. Except when explicitly measured, e.g., in phantom experiments, an approximate value $T_2^* = T_2/2$ was typically assumed.

Conclusion

Simulation software, validated against analytical, *in vitro* and *in vivo* results, provided organ-specific limits where dual-pathway PSIF-FISP sampling is TNR-superior to dual-FISP sampling. The results presented here are expected to help guide one's choice of pulse sequence and imaging parameters for PRF thermometry.

Author Manuscript Author Manuscript Author Manuscript Author Manuscript

Acknowledgements

Financial support from NIH grants R25CA089017, R01EB010195, R21EB019500 and P41EB015898 is duly acknowledged; content is solely the responsibility of the authors and does not necessarily represent the official views of the NIH.

References

1. Jolesz FA, Bleier AR, Jakab P, Ruenzel PW, Huttl K, Jako GJ. MR imaging of laser-tissue interactions. Radiology. 1988; 168(1):249–253. [PubMed: 3380968]
2. Parker DL, Smith V, Sheldon P, Crooks LE, Fussell L. Temperature distribution measurements in two-dimensional NMR imaging. Med Phys. 1983; 10(3):321–325. [PubMed: 6877179]
3. De Poorter J, De Wagter C, De Deene Y, Thomsen C, Stahlberg F, Achten E. Noninvasive MRI thermometry with the proton resonance frequency (PRF) method: in vivo results in human muscle. Magnetic resonance in medicine. 1995; 33(1):74–81. [PubMed: 7891538]
4. Ishihara Y, Calderon A, Watanabe H, Okamoto K, Suzuki Y, Kuroda K, Suzuki Y. A precise and fast temperature mapping using water proton chemical shift. Magnetic resonance in medicine. 1995; 34(6):814–823. [PubMed: 8598808]
5. Peters RD, Hinks RS, Henkelman RM. Ex vivo tissue-type independence in proton-resonance frequency shift MR thermometry. Magnetic resonance in medicine. 1998; 40(3):454–459. [PubMed: 9727949]
6. Rieke V, Butts Pauly K. MR thermometry. Journal of magnetic resonance imaging : JMRI. 2008; 27(2):376–390. [PubMed: 18219673]
7. McDannold N. Quantitative MRI-based temperature mapping based on the proton resonant frequency shift: review of validation studies. International journal of hyperthermia : the official journal of European Society for Hyperthermic Oncology, North American Hyperthermia Group. 2005; 21(6):533–546.
8. Celicanin Z, Auboiroux V, Bieri O, Petrusca L, Santini F, Viallon M, Scheffler K, Salomir R. Real-time method for motion-compensated MR thermometry and MRgHIFU treatment in abdominal organs. Magnetic resonance in medicine. 2014; 72(4):1087–1095. [PubMed: 24243500]
9. Madore B, Panych LP, Mei CS, Yuan J, Chu R. Multipathway sequences for MR thermometry. Magnetic resonance in medicine. 2011; 66(3):658–668. [PubMed: 21394774]
10. Panych, LP., Chu, R., Mei, C-S., Wang, G., Hoge, WS., Toews, M., Madore, B. Optimization of Dual-Pathway Unbalanced Steady-State Sequences for Robust Temperature Imaging. Salt Lake City, UT, USA: 2013. p. 4300
11. Bruder H, Fischer H, Graumann R, Deimling M. A new steady-state imaging sequence for simultaneous acquisition of two MR images with clearly different contrasts. Magn Reson Med. 1988; 7(1):35–42. [PubMed: 3386520]
12. Cheng, C-C., Mei, C-S., Aksit Ciris, P., Mulkern, RV., Balasubramanian, M., Chung, H-W., Chao, T-C., Panych, LP., Madore, B. Simultaneous frequency and T2 mapping, applied to thermometry and to susceptibility-weighted imaging. Toronto, Canada: 2015. p. 333
13. Hanicke W, Vogel HU. An analytical solution for the SSFP signal in MRI. Magnetic resonance in medicine. 2003; 49(4):771–775. [PubMed: 12652550]
14. Zur Y, Stokar S, Bendel P. An analysis of fast imaging sequences with steady-state transverse magnetization refocusing. Magnetic resonance in medicine. 1988; 6(2):175–193. [PubMed: 3367775]
15. Gyngell ML. The steady-state signals in short-repetition-time sequences. Journal of Magnetic Resonance (1969). 1989; 81(3):474–483.
16. Gudbjartsson H, Patz S. The Rician distribution of noisy MRI data. Magnetic resonance in medicine. 1995; 34(6):910–914. [PubMed: 8598820]
17. de Bazelaire CM, G. D, Rofsky NM, Alsop DC. MR imaging relaxation times of abdominal and pelvic tissues measured in vivo at 3.0 T: preliminary results. Radiology. 2004; 230(3):652–659. [PubMed: 14990831]

Author Manuscript Author Manuscript Author Manuscript Author Manuscript

18. Ding J, Xing W, Wu D, Chen J, Pan L, Sun J, Xing S, Dai Y. Evaluation of Renal Oxygenation Level Changes after Water Loading Using Susceptibility-Weighted Imaging and T2* Mapping. Korean J Radiol. 2015; 16(4):827–834. [PubMed: 26175582]
19. Cheng, C-C., Chung, H-W., Chao, T-C., Madore, B. Simultaneous relaxometry and susceptibility imaging in the brain. Salt Lake City, Utah, USA: 2013. p. 4216
20. Wansapura JP, Holland SK, Dunn RS, Ball WS Jr. NMR relaxation times in the human brain at 3.0 tesla. Journal of magnetic resonance imaging : JMRI. 1999; 9(4):531–538. [PubMed: 10232510]
21. Mädler, B., Harris, T., L., MA. Proceedings of the ISMRM 14th Scientific Meeting. Seattle: 2006. 3D-Relaxometry - Quantitative T1 and T2 Brain Mapping at 3T.; p. 958Proceedings of the ISMRM 14th Scientific Meeting
22. Lee, CE., Baker, EH., M., TD. Proceedings of the ISMRM 14th Scientific Meeting. Seattle: 2006. Normal Regional T1 and T2 Relaxation Times of the Brain at 3T.; p. 959Proceedings of the ISMRM 14th Scientific Meeting
23. Lewa CJ, Majewska Z. Temperature relationships of proton spin-lattice relaxation time T1 in biological tissues. Bulletin du cancer. 1980; 67(5):525–530. [PubMed: 6260272]
24. Cline HE, Hynynen K, Hardy CJ, Watkins RD, Schenck JF, Jolesz FA. MR temperature mapping of focused ultrasound surgery. Magnetic resonance in medicine. 1994; 31(6):628–636. [PubMed: 8057815]
25. Matsumoto R, Oshio K, Jolesz FA. Monitoring of laser and freezing-induced ablation in the liver with T1-weighted MR imaging. Journal of magnetic resonance imaging : JMRI. 1992; 2(5):555–562. [PubMed: 1392248]
26. Graham SJ, Bronskill MJ, Henkelman RM. Time and temperature dependence of MR parameters during thermal coagulation of ex vivo rabbit muscle. Magnetic resonance in medicine. 1998; 39(2):198–203. [PubMed: 9469702]
27. Bazrafshan B, Hübner F, Farshid P, Larson MC, Vogel V, Mäntele W, Vogl TJ. A liver-mimicking MRI phantom for thermal ablation experiments. Medical Physics. 2011; 38(5):2674. [PubMed: 21776804]
28. Bloembergen N, Purcell EM, Pound RV. Relaxation Effects in Nuclear Magnetic Resonance Absorption. Physical Review. 1948; 73(7):679–712.
29. Parker DL. Applications of NMR imaging in hyperthermia: an evaluation of the potential for localized tissue heating and noninvasive temperature monitoring. IEEE transactions on bio-medical engineering. 1984; 31(1):161–167. [PubMed: 6724602]
30. Bottomley PA, Foster TH, Argersinger RE, Pfeifer LM. A review of normal tissue hydrogen NMR relaxation times and relaxation mechanisms from 1-100 MHz: dependence on tissue type, NMR frequency, temperature, species, excision, and age. Med Phys. 1984; 11(4):425–448. [PubMed: 6482839]

Author Manuscript
Author Manuscript
Author Manuscript
Author Manuscript

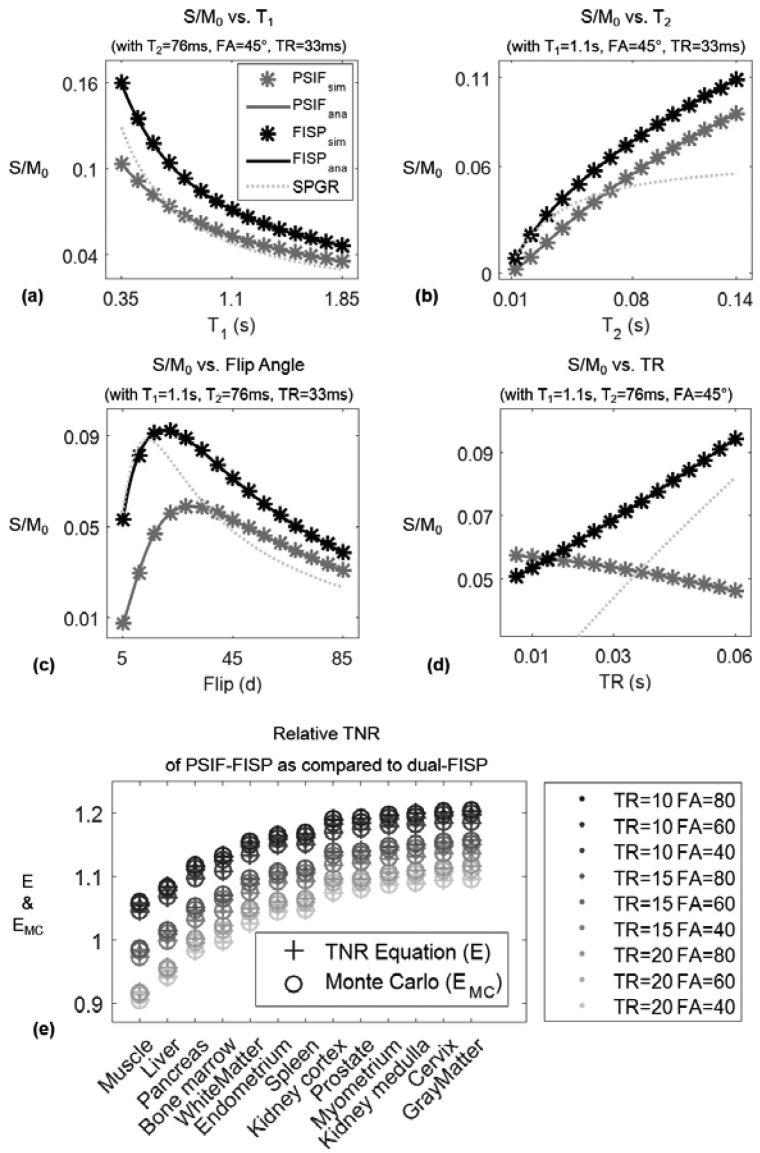


Figure 1.

(a-d) Dual-pathway PSIF and FISP signal simulations and analytical solutions, with $R_2'=0$, as a function of T_1, T_2, θ, and TR. Simulations and analytical solutions show excellent agreement. SPGR signal is also shown for comparison (at $TE = 3/4\ TR$, $T_2=T_2^*$), and remains below FISP signal levels in all cases. (e) Relative TNRs from TNR equations vs. Monte Carlo experiments for various tissues and acquisition parameters, also agree very well.

Author Manuscript
Author Manuscript
Author Manuscript
Author Manuscript

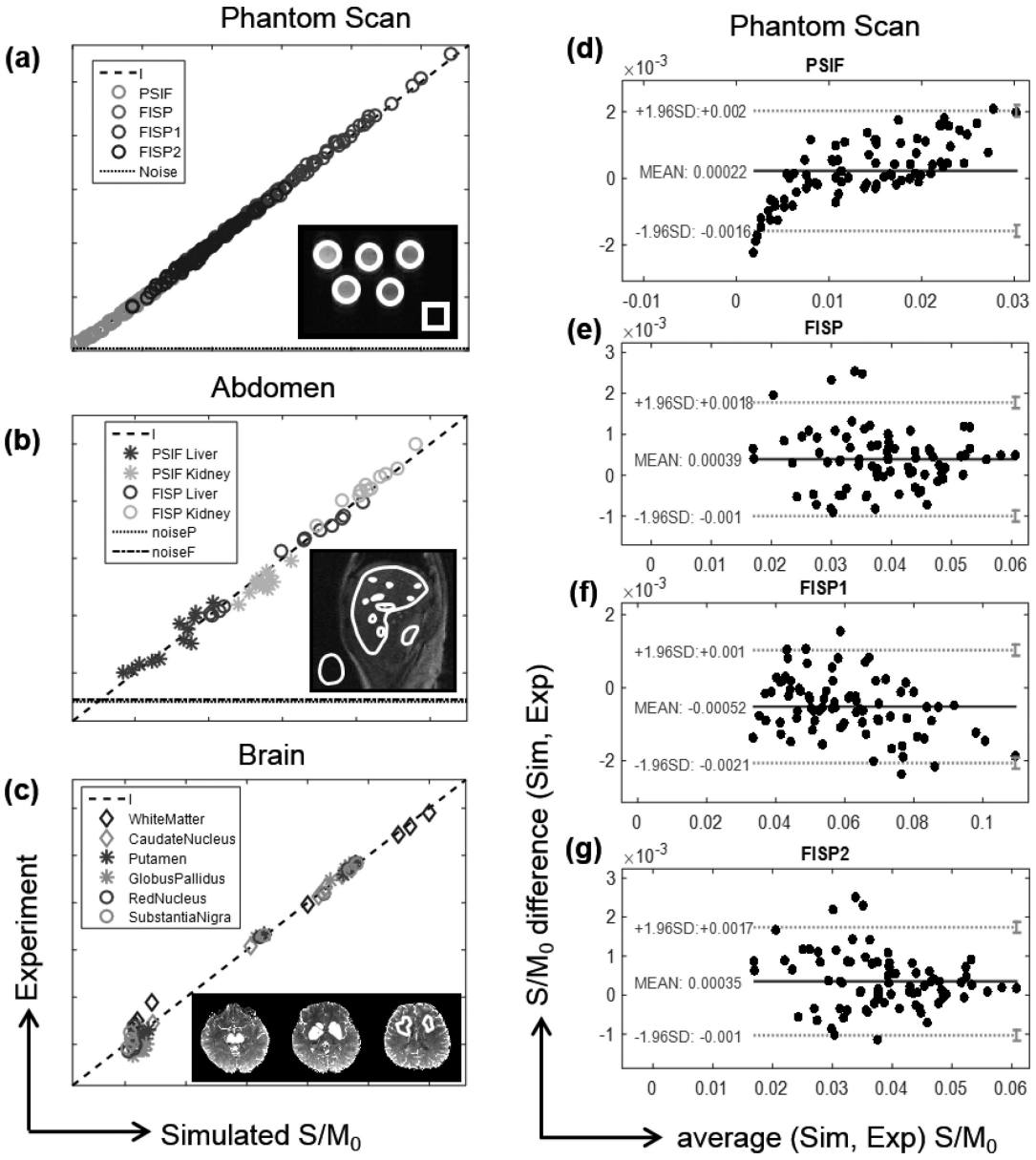


Figure 2.

Dual-pathway simulations vs. in vivo experiments, with $R_2' \neq 0$. Simulations agree well with experimental results. (a-c) Experimental and simulated results are compared for each pathway relative to the identity line, with phantom, abdomen, brain and noise ROIs also shown on sample images. (d-g) The phantom results from (a) are also displayed here in the form of Bland-Altman plots.

Author Manuscript Author Manuscript Author Manuscript Author Manuscript

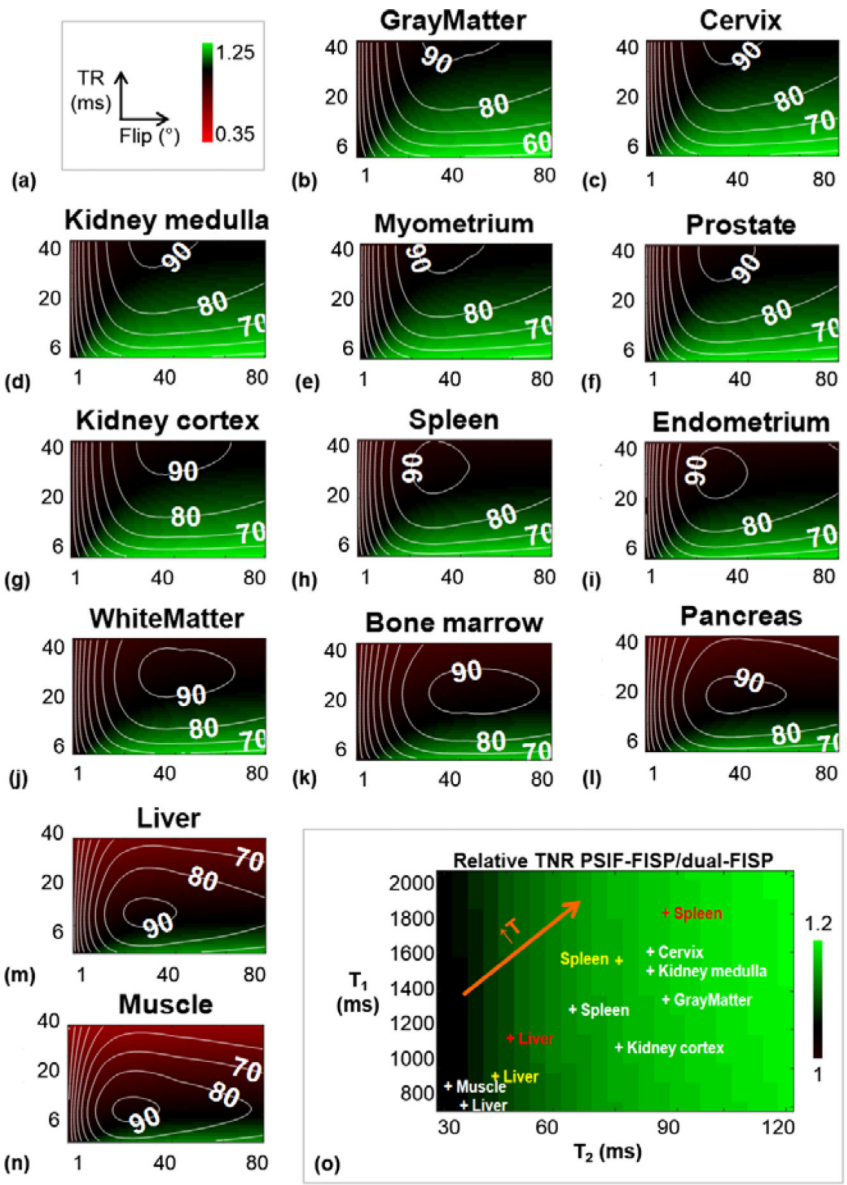


Figure 3.

(a-o) E, the relative TNR of PSIF-FISP vs. dual-FISP acquisitions, for various tissues and acquisition parameters. Green: higher TNR with PSIF-FISP. Red: higher TNR with dual-FISP. Contours: E_{global}, TNR with PSIF-FISP (at each TR and FA parameter set), relative to the maximum achievable TNR with dual-FISP across all tested TR and FA parameter sets (as a percentage). (o) Relative TNR of PSIF-FISP vs. dual-FISP, as a function of T_1 and T_2 (at TR = 15ms, FA = 60°). White: Relative TNR at baseline tissue T_1 and T_2. TNR increases with heating as tissue T_1 and T_2 increase. The effect of 20 °C heating is shown for the liver and spleen, for 1% and 2% per °C changes in T_1 and T_2, in yellow and red, respectively.

Author Manuscript Author Manuscript Author Manuscript Author Manuscript

Table 1

Relaxation rate values, at 3T, assumed for simulations presented in Figs 1-3

	T_1 (ms)	T_2 (ms)	T_2*(ms)	Fig(s)
Top Left Tube[1]	395	30	29	2a, 2d-g
Top Mid Tube[1]	571	34	33	2a, 2d-g
Top Right Tube[1]	835	45	42	2a, 2d-g
Bottom Left Tube[1]	945	49	45	2a, 2d-g
Bottom Right Tube[1]	1460	55	51	2a, 2d-g
Liver[2]	809[5]	34[5]	17[4]	2b, (1e, 3)[4]
Kidney Cortex[2]	1142[5]	76[5]	59[6]	2b, (1e, 3)[4]
Kidney Medulla[2]	1545[5]	81[5]	25[6]	2b, (1e, 3)[4]
White Matter[3]	803[7]	57±4	49±4	2c, (1e, 3)[4]
Caudate Nucleus[3]	1563[8]	52±6	43±7	2c
Putamen[3]	1403[8]	42±7	39±4	2c
Globus Pallidus[3]	951[7]	29±15	28±3	2c
Red Nucleus[3]	1260[8]	35±16	33±2	2c
Substantia Nigra[3]	1421[8]	33±18	30±2	2c
Gray Matter (all)[2]	1331[9]	86[9]	-	(1e, 3)[4]
Cervix[2]	1616[5]	83[5]	-	(1e, 3)[4]
Prostate[2]	1597[5]	74[5]	-	(1e, 3)[4]
Myometrium[2]	1514[5]	79[5]	-	(1e, 3)[4]
Endometrium[2]	1453[5]	59[5]	-	(1e, 3)[4]
Spleen[2]	1328[5]	61[5]	-	(1e, 3)[4]
Muscle[2]	898[5]	29[5]	-	(1e, 3)[4]
Pancreas[2]	725[5]	43[5]	-	(1e, 3)[4]
Bone Marrow[2]	586[5]	49[5]	-	(1e, 3)[4]

[1] Rates determined experimentally

[2] Rates obtained from literature

[3] T_1 obtained from literature, T_2 and T_2* from fitting

[4] Simulations assumed T_2*= T_2 / 2

[5] Values from Ref. (17)

[6] (18)

[7] (21)

[8] (22)

[9] Ref. (20)

Author Manuscript

Author Manuscript

Author Manuscript

Author Manuscript

Author Manuscript

Author Manuscript

Author Manuscript

Author Manuscript

Table 2

Imaging parameters for the experimental results presented in Fig. 2

	Flip (°)	TR (ms)	TE_{PSIF} (ms)	TE_{FISP} (ms)
Phantom Scan1	10	13	3.1	8.1
Phantom Scan2	10	20	3.1	15.1
Phantom Scan 3	10	30	3.1	25.1
Phantom Scan 4	10	40	3.1	35.1
Phantom Scan 5 to 8	20	Same TR and TEs as Phantom Scan 1 to 4		
Phantom Scan 9 to 12	30	Same TR and TEs as Phantom Scan 1 to 4		
Phantom Scan 13 to 16	40	Same TR and TEs as Phantom Scan 1 to 4		
Abdomen V1 (ETL= 2)	30	9	3.4	6.3
Abdomen V1 (ETL= 4)	30	11	2.4	6.5
Abdomen V1 (ETL= 6)	30	14	4.5	10
Abdomen V1 (ETL= 8)	30	17	3.7	10.6
Abdomen V2 (ETL= 2)	30	8	3	5.5
Abdomen V2 (ETL= 4)	30	11	2.1	5.9
Abdomen V2 (ETL= 6)	30	14	4.1	9.3
Abdomen V2 (ETL= 8)	30	17	3.4	9.9
Abdomen V3 (ETL= 2)	30	9	3	5.5
Abdomen V3 (ETL= 4 to 8)	Same Flip, TR, and TEs as Abdomen V2 (ETL = 4 to 8)			
Brain V4 (# slices = 40)	25	40	6.6 15.8 25.3 35.1	3.8 13.1 22.6 32.3
Brain V5 (# slices = 42)	25	50	8.2 19.7 31.6 45.0	4.3 15.8 27.8 40.1
Brain V6 (# slices = 44)	30	50	7.0 16.5 26.2 35.9 45.7	3.9 13.5 23.2 32.9 42.7
Brain V7 (# slices = 40)	25	50	10.3 21.4 32.5 43.5	6.5 17.5 28.6 39.7